

Electron Optical Observation of Magnetic Fields

By L. Marton and S. H. Lachenbruch

The electron optical analog of the "Schlieren" method may be used to explore electro-magnetic fields where conventional methods fail. Furthermore, a related shadow method, especially suitable for the quantitative evaluation of such fields, has been found.

Properties of the Schlieren patterns produced by a magnet consisting of two point poles are predicted by a mathematical analysis. An experimental Schlieren pattern, produced by a magnetized recording wire, is interpreted qualitatively and compared with a powder pattern.

The related shadow method is applied to the magnetized wire. The experimental data are shown to agree well with theoretical formulas derived from this hypothesis and yield reasonable numerical values for the field strength and for the separation of the point poles to which each magnetized region is assumed equivalent.

I. Introduction

In a short communication¹ it was pointed out that, in close analogy to the light optical Schlieren effect, by means of which small variations of optical density can be observed,² an electron optical Schlieren effect can be produced and used for the observation of electrostatic and magnetic fields of minute extent. Subsequent experiments have revealed, in addition, a related and equally sensitive method that utilizes the same apparatus as the Schlieren method but is somewhat preferable for the quantitative evaluation of such fields. In contrast with the dark-field Schlieren intensity patterns, this related method involves measurements on deformed shadows against a bright background.

As one illustration of the value of the Schlieren and related methods, this paper deals with a detailed description and analysis of the observation of the magnetic fields of magnetized wires used for recording purposes. Such wires can be magnetized by short current pulses by means of the conventionally built magnetic recording heads. Although such recording wires have been used for several years, there was little information available on the extent of the magnetized regions and on the intensity of the magnetic field produced. The extent of the magnetization can be determined

experimentally either by means of the Schlieren effect, or by means of a powder pattern produced by extremely fine iron dust or a ferromagnetic colloid.³ As regards the value of the field strength, its determination by means of the conventional methods seems to be highly impractical because of the very small dimensions of the magnetized region. Under these conditions the best approach to the problem seems to be the use of electrons for the exploration of the fringe field extending from each magnetized region.

A quantitative evaluation of this inhomogeneous fringe field is based on the deflection of the electrons produced by the field. Measurements on the configurations produced by this deflection are substituted into theoretical formulas derived from the field distribution function.

The final quantitative results are based on the assumption that the field in each magnetized region is the same as that produced by two equal and opposite *point poles* a finite distance apart. The observations have shown that this hypothesis explains with sufficient accuracy all observed facts. In the analysis that follows, for a first approximation it is assumed that the field is that of an ideal magnetic dipole (infinitesimal pole separation), while in section V the accuracy is improved by

¹ L. Marton, J. Appl. Phys. **19**, 687 (1948).

² See, e. g., H. Schardin, Toepler's Schlieren method, Translation 156, David Taylor Model Basin, U. S. Navy (July 1947).

³ Irvin L. Cooter, *Elect. Eng.* **68**, 433 (1949); (Digest of AIEE Paper No. 48-237).

generalizing this hypothesis to take into account the finite lengths of the magnetized regions.

As the basis of the analytical results, therefore, section II deals with a general mathematical discussion of the properties of electron paths in the equatorial plane of an ideal magnetic dipole. In subsequent sections these results are used for the theoretical prediction of Schlieren and related patterns and for the derivation of formulas for the field intensity in terms of pattern measurements and experimental constants. Experimental results are compared with predictions. The theoretical formulas derived are modified to take magnet length into account. Finally, calculations are carried out, using quantitative experimental data, for the determination of the magnitude of the field and of the effective pole separation, and for a partial check on the validity of the underlying theoretical assumptions.

II. Trajectories of Electrons in Dipole Field

1. Exact Analysis

We assume the presence of a magnetic field produced by an ideal dipole. Figure 1 is the coordinate diagram of the dipole field in its equatorial plane. The origin is the center of the dipole, which is normal to the page with its north

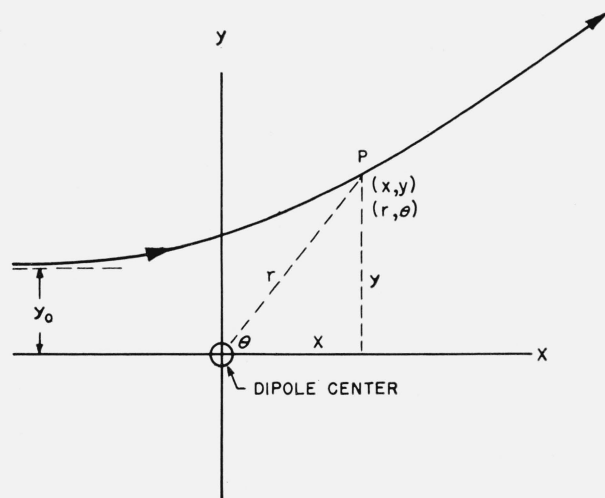


FIGURE 1. Coordinate diagram for electron path in equatorial plane of dipole.

pole below it, i. e., its sense is such that electrons are repelled when y and dx/dt are positive. The x -axis is placed parallel to the initial direction of motion, and the initial ordinate, y_0 , is the distance parameter, that locates the incident ray. Polar (r, θ) and rectangular (x, y) coordinates will be used interchangeably.

The magnetic field in the equatorial plane of a dipole varies inversely as the cube of the distance $r = \sqrt{x^2 + y^2}$ from the dipole center:

$$H = M/\mu' r^3, \quad (1)$$

where M is the magnetic moment and μ' the permeability of the medium, which is unity for a vacuum when emu are used. If A is the radius of curvature of the path at any point, A is inversely proportional to H , and it follows from eq 1 that

$$r^3/A = B = \text{constant}, \quad (2)$$

which has the dimensions of area and can be shown to be given by

$$B = Me/mv = M\sqrt{e/2mV}, \quad (3)$$

where v , V , e , m are the speed, accelerating potential, charge, and mass of the electron. We take \sqrt{B} as a normalizing unit of length and indicate by *capital letters* the normalized coordinates

$$Y = y/\sqrt{B}, \quad X = x/\sqrt{B}, \quad R = r/\sqrt{B}. \quad (4)$$

The length \sqrt{B} turns out to be the radius of the one circular trajectory possible in this system.

The analytical equation of the trajectories of electrons entering such a field have been derived⁴ in terms of elliptic integrals. In normalized polar coordinates (R, θ) this exact solution may be expressed as follows:

$$\theta = \theta(R, Y_0) = \pi - G(\pi/4, Y_0) \pm G(\psi, Y_0), \quad (5)$$

where

$$\psi = \psi(R, Y_0) = (1/2) \arccos [(Y_0 R + 1)/R^2]; \quad (6)$$

$$F(\psi, k) = \text{elliptic integral of first kind}; \quad (7)$$

⁴ See, e. g., C. Graef and S. Kusaka, J. Math. Phys. **17**, 43 (1938).

$$k = \sqrt{8/(Y_0^2 + 4)};$$

$$G(\psi, Y_0) = \begin{cases} \psi + (kY_0/\sqrt{8})F(\psi, k), & \text{when } Y_0 \geq 2; \\ \psi - \pi/2 + (k|Y_0|/\sqrt{8})\{F(\psi, k) - F(\pi/2, k)\}, & \text{when } Y_0 \leq -2; \\ \psi + (Y_0/\sqrt{8})F[\arcsin(k \sin \psi), 1/k], & \text{when } 0 \leq Y_0 \leq 2; \end{cases} \quad (8)$$

and a somewhat more complex but similar expression when $-2 < Y_0 < 0$.

The quantity $Y_0 = y_0/\sqrt{B}$, which is the only parameter appearing in the above solution, is dimensionless and contains all the given conditions of the problem, viz., the initial ordinate y_0 , moment M , and electron energy V . For a monochromatic parallel incident beam, V and M , and therefore B , are fixed, and y_0 is the basic parameter of the system.

For such a parallel incident beam, the resulting family of trajectories is shown in figure 2 for equally spaced values of Y_0 . The cases $Y_0 = -2$ and $Y_0 = 0$ give degenerate forms: for $Y_0 = -2$ the electron spirals without limit, approaching the unit circle $R=1$ as asymptote; and for $Y_0 = 0$, i. e., for an electron initially headed for the dipole center, the path is an equilateral hyperbola tangent to that unit circle, having the two coordinate axes as asymptotes and giving a deflection $\tilde{\theta} = \pi/2$.

The *caustic* curve (shown by dot-dashed curve marked "Envelope" in the fig.) is the locus of points for which $dY/dY_0 = 0$. This curve executes a spiral similar in form to the $Y_0 = -2$ trajectory, and approaches as asymptote the circle whose equation is $R = \sqrt{2} - 1 = 0.4$, whereas for large X it approaches a cubic curve.

The *angular deflection*, $\tilde{\theta}$, which is positive for all Y_0 , is given by the inclination of the final asymptote, the initial asymptote being horizontal. Setting $R = \infty$, eq 6 and 5 give for the final deflection

$$\tilde{\theta} = \theta(\infty, Y_0) = \pi - 2 G(\pi/4, Y_0), \quad (9)$$

where G is defined by eq 8.

The equation of the *final asymptote* of any trajectory may be obtained as follows: The two asymptotes of a trajectory must intersect on its line of symmetry, which by eq 5 is the radial line,

$$\theta = \pi - G(\pi/4, Y_0) = \pi/2 + \tilde{\theta}/2, \quad (10)$$

the latter form being obtained from eq 9. But the equation of the initial asymptote is $Y = Y_0$, so that the intersection is at

$$(Y = Y_0, X = -Y_0 \tan \tilde{\theta}/2 = -Y_0[\csc \tilde{\theta} - \cot \tilde{\theta}]). \quad (11)$$

The slope of the final asymptote is $\tan \tilde{\theta}$ by definition. From these it follows that the final asymptote has the equation,

$$Y = Y_0 \sec \tilde{\theta} + X \tan \tilde{\theta}, \text{ or } y = y_0 \sec \tilde{\theta} + x \tan \tilde{\theta}. \quad (12)$$

Here the deflection $\tilde{\theta}$ is itself a function of Y_0 and is given analytically by eq 9. The Y -intercept, \tilde{Y} , of a final asymptote is thus

$$\tilde{Y} = Y_0 \sec \tilde{\theta}, \text{ or } \tilde{y} = y_0 \sec \tilde{\theta}. \quad (13)$$

The final asymptotes (eq 12) of the main trajectories of figure 2 are replotted in figure 3, and each is extended back to the point (eq 11) where it intersects the horizontal initial asymptote. These asymptotes possess an envelope (dot-dashed curve), which is, of course, asymptotic to the caustic of figure 2 for large X , but whose only significant intersection with the Y -axis is in a lower branch, which corresponds to a negative Y :

$$Y = -2.93, \quad Y_0 = -2.58. \quad (14)$$

2. Small-Deflection Approximations

The results of the experiments to be described later indicate conditions (dipole strength and voltage) such that the normalizing factor \sqrt{B} is small compared with the radius of the magnetized wire. The quantitative results to be presented in section V lead to a value of \sqrt{B} of the order of $1/15$ of the wire radius. This would imply that, in practice, trajectories corresponding to $|Y_0| < 15$ have little physical significance here. For experimental purposes we shall be concerned chiefly with trajectories so far from the dipole center that the deflection is very small (well beyond the range of figs. 2 and 3). Thus approximate analytical expressions for large $|Y_0|$ will be experimentally useful as well as much simpler than those involving elliptic integrals, although the exact expressions could be called for in exactly similar problems with different physical parameters.

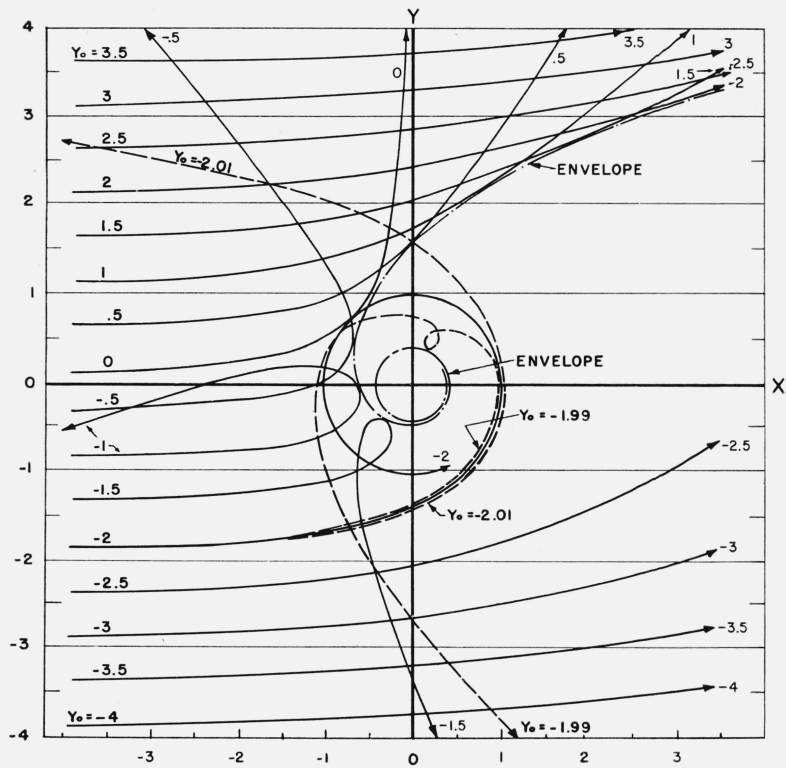


FIGURE 2. Trajectories of electrons in equatorial plane of dipole, parallel incidence (normalized coordinates).
Curve marked "Envelope" is the caustic curve.

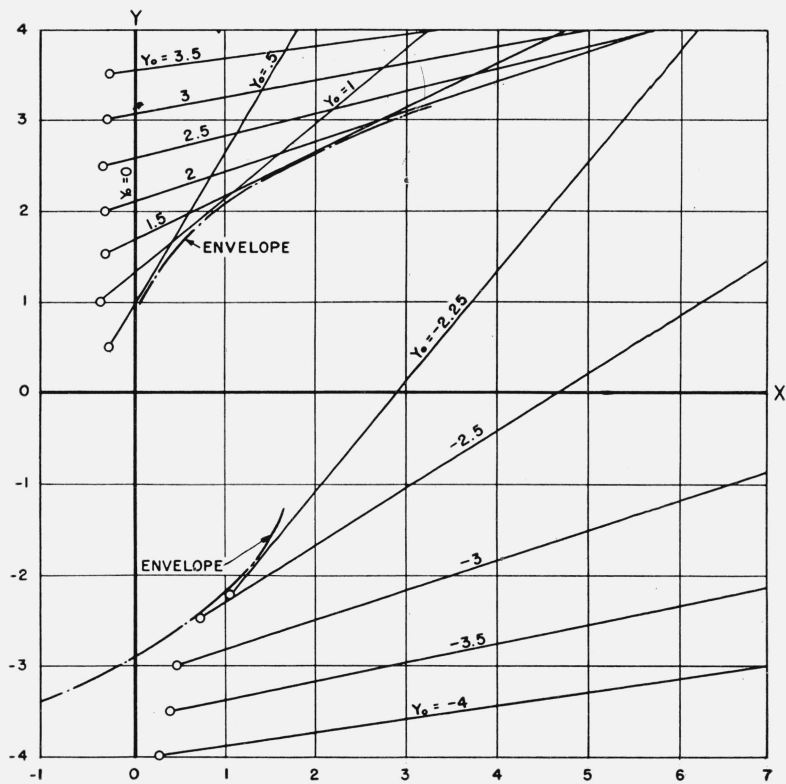


FIGURE 3. Final asymptotes of the trajectories of figure 2.

The elliptic integral $F(\psi, k)$ can be expanded in even powers of k as

$$F(\psi, k) = \psi + \frac{k^2}{4}(\psi - \sin \psi \cos \psi) + O(k^4). \quad (15)$$

For large $|Y_0|$, by eq 15, 5, 6, and 8, the equations of the (almost straight) trajectories can be shown to simplify to

$$R = Y_0 / \{ \sin(\theta - 1/Y_0^2) - 1/Y_0^2 \}. \quad (16)$$

On setting $R = \infty$ one then obtains for the small final deflection angle

$$\tilde{\theta} \approx 2/Y_0^2. \quad (17)$$

The equation (eq 12) of the asymptote becomes approximately

$$Y = Y_0 + \tilde{\theta} X = Y_0 + 2X/Y_0^2, \quad (18)$$

and its Y -intercept (eq 13) becomes

$$\tilde{Y} \approx Y_0. \quad (19)$$

The latter implies that the two asymptotes of a trajectory intersect approximately on the Y -axis when $|Y_0|$ is large.

Analogous results for a magnet of finite length are given in section V.

III. Schlieren Observation of Intensity Patterns

1. Description of the Method

In its simplest form the electron optical Schlieren effect can be observed by using an electron source, the image of which is projected on a conveniently placed stop by means of an electron optical lens. This stop blocks all direct rays. In the absence of any scattering object or deflecting field in the space between source and lens, there is no radiation reaching the space beyond the stop. If, however, in the space between source and lens there exists a variation of the electromagnetic index of refraction (or there is some material present that scatters the electrons), the rays will be deflected from their normal pattern and will form a dark-field image in the image space beyond the stop. This image is obviously a pictorial representation of the deflections in the plane conjugate to the image plane with respect to the lens.

Although this description of the Schlieren effect is limited to the use of a single lens, it is obvious that the use of more than one lens may often prove advantageous. Two special cases of more than passing interest may be noted here. One is the case of two lenses, forming the image of the source with a parallel beam in the space between the two lenses, and the other is the case of a compound instrument producing high magnification of the Schlieren image. In the first case, the object can be placed in the parallel beam, which has the advantage of a rather uniform illumination. In the second case, a compound instrument is used when the variations of the electromagnetic index of refraction are of such minute extent that a microscope system is needed for the observation. It is obvious that a great number of combinations of optical elements can be adapted to the needs of the experiment for the many possible applications of the Schlieren effect (some of which are listed in our previous short communication; see footnote 1).

It is not our intention here, however, to describe all the possible variations of the experimental arrangement. Rather this section deals with the special application of the method to the observation of the magnetic field of the magnetized wire described in the introduction (sec. I). After a theoretical discussion of the effect, based on the results of section II and intended for general reference, the detailed laboratory procedure and experimental results are described.

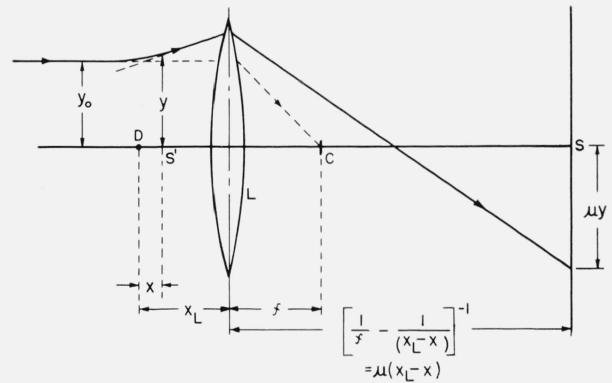


FIGURE 4. Electron optical diagram of Schlieren apparatus.

2. Theoretical Analysis

The electron optical arrangement for obtaining Schlieren images of the inhomogeneity produced by a dipole is shown schematically in figure 4, whose plane is the equatorial plane of the dipole,

D. A converging lens, *L*, is placed at a distance X_L sufficiently far beyond *D* so that all electron trajectories may be considered as coinciding with their asymptotes there. In the absence of the deflecting field, a parallel beam of electrons will be blocked by the center stop, *C*, placed at the lens focus. Rays deflected sufficiently by the dipole field pass the stop and are collected on a fluorescent screen, *S*.

It is obvious from figure 4 that the distribution of electrons on the screen, *S*, is an image of the *virtual* distribution that is obtained in the *plane*, *S'*, *conjugate to that of the screen* by extrapolating all the final asymptotes back to that plane. Thus, if the plane *S'* is at a distance *X* to the right of the dipole, an electron of initial ordinate Y_0 will have at the screen an ordinate μY , where *Y* is given by eq 12, and μ is the magnification produced by the lens; and the properties of the distribution on the screen may be predicted from a study of the intersections of the asymptotes of

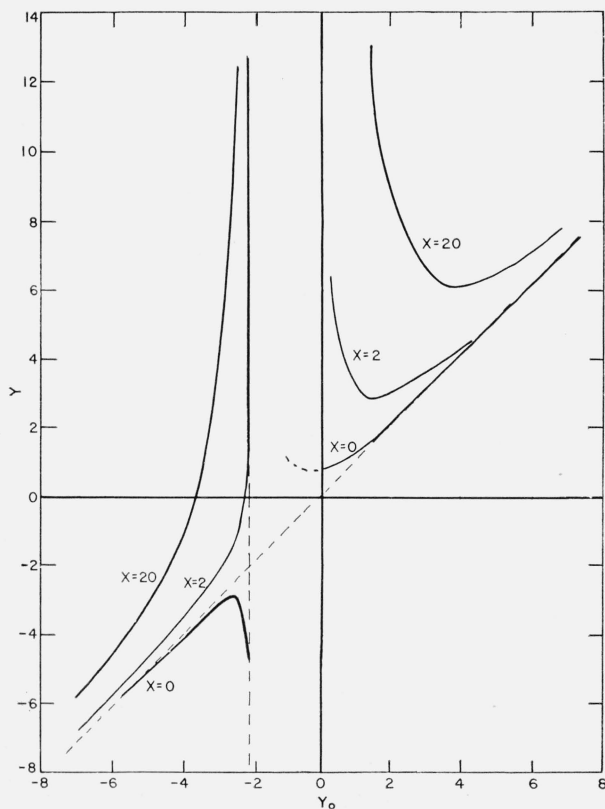


FIGURE 5. Distance *Y* of final trajectory asymptotes of figure 3 from optic axis at fixed distances *X* beyond dipole, as function of initial distance parameter Y_0 .

figure 3 with a vertical line at abscissa *X*. (In the experiments $X=0$.)

If the screen, lens, and dipole positions, and therefore the conjugate abscissa *X*, are fixed, the position *Y* (more precisely, μY) of any electron on the screen is a unique function of its initial ordinate Y_0 , as given by eq 12 and figure 3. Figure 5 is a plot of *Y* versus Y_0 for several different values of *X*. For large $|Y_0|$ all the curves approach the 45° line $Y=Y_0$. It is obvious that the *inverse* function defined thereby (Y_0 as function of *Y*, for fixed *X*) is multiple-valued; i. e., in general, the electrons reaching the screen at a given ordinate *Y* may originate in any of several initial ordinates Y_0 .

The distribution of electrons on the screen is then obtained as follows: In a parallel, monochromatic incident beam of uniform linear current density σ_0 , the total electron current in an elementary initial interval (Y_0, Y_0+dY_0) is $\sigma_0|dY_0|$. These electrons form at the screen an elementary interval $(Y, Y+dY)$, so that they contribute to the current density at this point on the screen an amount

$$\sigma_i = \sigma_0 |dY_0/dY|. \quad (20)$$

Hence the relative current density σ/σ_0 at the screen, which serves as a measure of the intensity of the electron beam at any point, *Y*, on the screen, is given by

$$\frac{\sigma}{\sigma_0} = \sum \frac{\sigma_i}{\sigma_0} = \sum |dY_0/dY| = \sum \frac{1}{|dY/dY_0|}, \quad (21)$$

where the summation is over all values of Y_0 which correspond to the given value of *Y*, i. e., over all branches of the multiple-valued function described above. Graphically, the density function σ/σ_0 at any point *Y* on the screen is obtained from figure 5 by adding up the reciprocals of the absolute slopes of the appropriate curve at all points⁵ at which it has the ordinate *Y*.

The resulting distributions are plotted in figure 6 for the same fixed values of *X*. A point of infinite density appears at the value of *Y* corresponding to the ordinate of the caustic of figure 3 at each abscissa *X*; but the density approaches

⁵ The curves of figure 5 are not plotted in the region $-2.1 \leq Y_0 \leq 0$. In about three-fourths of this region, $\bar{\theta}$ lies between $\pi/2$ and $3\pi/2$, so that the electrons turn around and never reach the screen. In the remaining narrow interval $\bar{\theta}$ varies from $3\pi/2$ to ∞ and back; the curves, if plotted, would have an infinite number of branches of practically infinite slope dY/dY_0 , and so do not contribute appreciably to the distribution.

unity rapidly as $|Y|$ becomes large, indicating a rapid falling off to the uniform initial density, as modified only by the lens magnification effect. The value, or values, of Y_0 corresponding to any point on a curve of figure 6 may be determined with the aid of figure 5.

Under the conditions of the experiments about to be described, the phenomenon takes on a considerably simplified form, due to the following considerations:

(a) The Schlieren experiments were performed only for the case

$$X=0, \quad (22)$$

i. e., the case for which the dipole center itself is in the plane conjugate to that of the fluorescent screen. For this case the magnetized wire is imaged with the same magnification as the pattern surrounding it, and appears on the screen as a dark band across the pattern.

(b) Whereas figure 6 assumes an unlimited

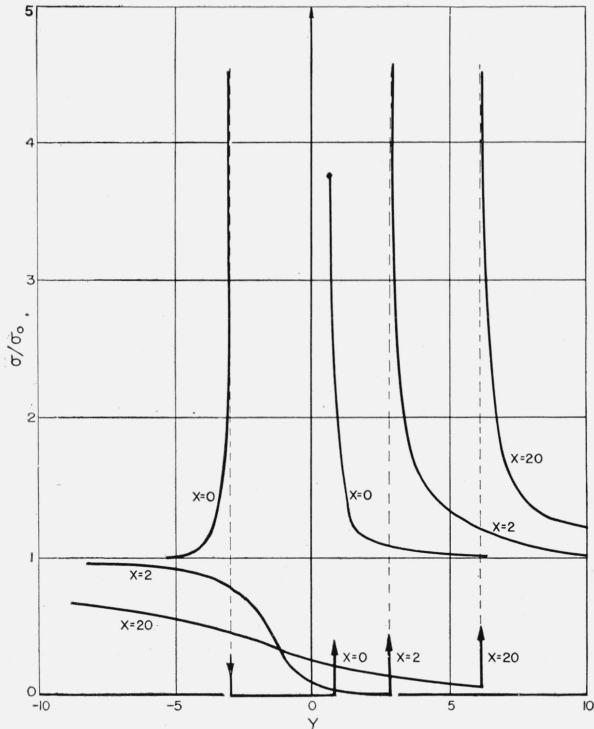


FIGURE 6. Distribution of virtual electron density σ —relative to density σ_0 in absence of dipole field—along line S' of figure 4, normal to optic axis at fixed distances X beyond dipole, based on extrapolated final asymptotes of initially parallel paths.

Actual density distribution on fluorescent screen S , conjugate to S' , is obtained by multiplying Y , and dividing σ/σ_0 , by magnification μ .

range of Y_0 , i. e., an infinitely wide and unobstructed initial beam, the effective Y_0 -range is actually limited by such factors as finite beam thickness, finite lens aperture, and the presence of the center stop.

(c) Values of Y_0 near zero are also excluded, due to the finite wire thickness. As noted in section II, 2, results indicate that the excluded central range is roughly the interval $-15 < Y_0 < 15$.

The effect of the Y_0 -range limitations (b) and (c) is to reduce to zero those intensity components due to the excluded values of Y_0 , without changing the intensity components elsewhere. The patterns thus have a finite extent, measurements on which may be used for a rough quantitative determination of the field under ideal experimental conditions.

Limitation (c), furthermore, permits a much simplified analytical treatment of the problem, with the aid of eq 17 and 18. For these large values of $|Y_0|$, eq 18 becomes the basic equation on which the distribution is based. In the general case this is a cubic in Y_0 , determining Y_0 as an at-most-three-valued function of Y . But under condition (a) above, for which eq 22 applies, eq 18 reduces to eq 19:

$$Y = \tilde{Y} \approx Y_0, \quad (23)$$

whence the density function (eq 21) reduces to

$$\sigma/\sigma_0 \equiv 1; \quad (24)$$

i. e., limitation (c) restricts us to regions far enough away from the dipole so that the initial uniform density is essentially unchanged.

At the same time, limitation (b) causes this density to fall off abruptly to zero at the values of Y corresponding to the outermost rays, as determined by beam width, lens aperture, stop size, etc. Thus, with its central portion hidden by the wire image in accordance with limitation (c), the pattern may be expected, in general, to extend out a certain distance on either side of the wire, as represented by the inequality

$$Y_{\min} \leq Y \leq Y_{\max}, \quad (25)$$

where Y_{\min} and Y_{\max} are functions of the physical parameters of limitation (b).

For example, where the lens aperture size is the most stringent limitation, by eq 18 and 23, Y_{\min} and Y_{\max} are given approximately as solutions of

$$\begin{aligned} Y_{\min} + 2X_L/Y_{\min}^2 + R_L &= 0, \\ Y_{\max} + 2X_L/Y_{\max}^2 - R_L &= 0, \end{aligned} \quad (26)$$

R_L being the radius of the aperture in the lens plane $X=X_L$. Or, when the physical size (radius R_c in normalized units, r_c in length units) of the center stop is the determining limitation, one obtains approximately

$$Y_{\min} \approx -\sqrt{2f/r_c}, \quad Y_{\max} \approx +\sqrt{2f/r_c}, \quad (27)$$

f being the focal length.

Analogous inequalities for the case of magnet of finite length are given in section V.

3. The Schlieren experiments

The experiments were carried out by means of a slightly modified electron microscope. This electron microscope, of horizontal design, consists of an electron gun, three magnetic lenses, and a fluorescent screen. The electron gun is identical with the one described in one of our previous communications⁶ and, for the purpose of this experiment, it has been operated at 40 kv. The lenses are of the conventional ironclad design, without internal polepieces, and have 10,000 turns of No. 23 copper wire each. The inner bore diameter of the iron enclosure is $\frac{5}{8}$ in., and the gap width is $\frac{1}{2}$ in. In most experiments only one lens of the instrument was used for producing the Schlieren image, and the other two lenses were not connected at all. The lens most used for the experiments is the projector lens of the electron microscope, thus reducing the whole instrument to the simplest instrumentation as described in section III, 1. In some experiments, however, the condenser lens of the instrument was switched on for the purpose of obtaining increased intensity of the image. As the condenser lens was used as a weak lens, it did not influence the essential optical arrangement, although it enhanced the available intensity. In most experiments the object consisted of a 0.0046-in. diameter cobalt-nickel-plated brass wire, placed at distances varying from $\frac{3}{4}$ to 2 in. from the lens center. On the image side of the lens was placed a center stop, consisting of a 0.040-in. diameter copper disk supported by two very fine metallic cross-wires (0.0013-in. diameter). The fluorescent screen for the observation of the image

⁶ L. Marton, *J. Appl. Phys.* **16**, 131 (1945).

was placed at a distance of about 13 in. from the lens center.

A typical Schlieren image from a magnetized wire is shown in figure 7, A. This particular wire was magnetized by short current pulses spaced at about 0.017 in. distance. The dark shadow of the wire is easily recognized in the image, surrounded by the bright Schlieren images. Such an image gives immediately a good qualitative picture of the extent of the magnetic field and allows judgment about the extent of the magnetization along the wire axis. A comparison with a powder pattern (see footnote 3) produced on the same wire permits an easy identification of the magnetized regions (fig. 7, B).

The equatorial planes of the alternately polarized dipoles of the wire correspond to lines of approximate symmetry drawn through the centers and peaks of the Schlieren images appearing in

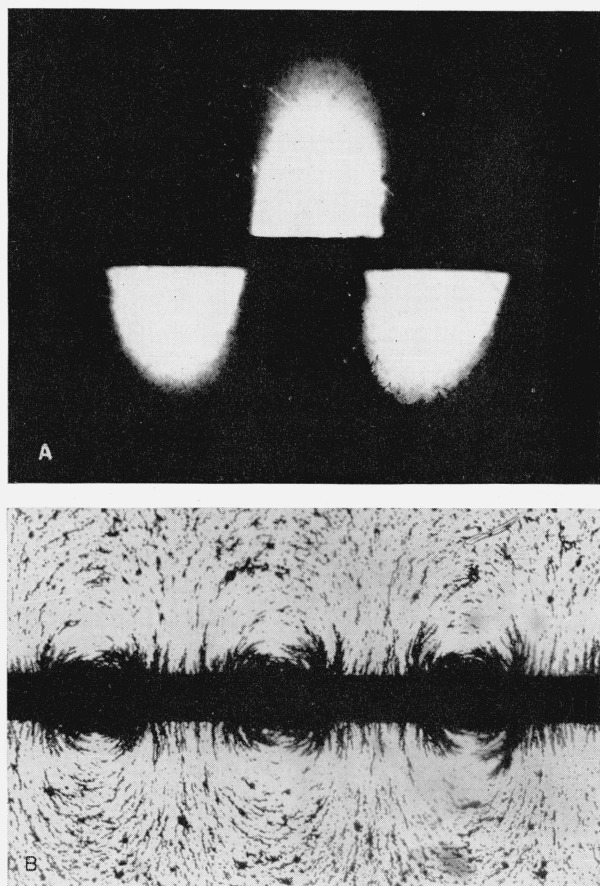


FIGURE 7. (A) A typical Schlieren pattern; total magnification of wire about $\times 150$. (B) Powder pattern identifying magnetized regions of same wire; total magnification about $\times 150$.

(Courtesy of Irvin L. Cooter; see footnote 3).

figure 7, A, on alternate sides of the wire image. The illumination appears approximately uniform, as predicted by eq 24, out to the extremity of the pattern, where it drops off to zero. In this particular image the pattern of any one dipole is visible beyond the wire on only one side of it, indicating an asymmetrical type of outer limitation on the final beam.

An observation made in the course of the experiments is worthy of mention. During the focusing of the image of the magnetized wire, it is found that the out-of-focus images of the wire are not straight. The image of the magnetized regions is displaced with respect to that of the nonmagnetized ones, and this displacement reverses on crossing the focus. The explanation of this phenomenon is rather obvious: when the lens is adjusted to focus the image of a plane closer to the lens than the actual object, the electrons passing by in a magnetized region are deflected with respect to those passing through a nonmagnetized region (see fig. 8, a). The result

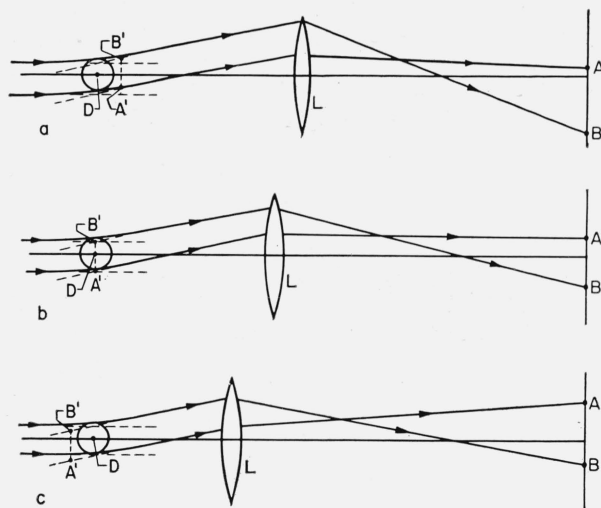


FIGURE 8. Optical diagram in an equatorial plane, showing method of focusing wire on screen.

(a) Wire too far from lens, image AB not centered; (b) wire in focus, image AB approximately centered; (c) Wire too close to lens, image AB not centered.

is that the image of the magnetized region appears displaced as compared with the nonmagnetized region. If the lens is adjusted to produce an image of a region beyond the actual object (see fig. 8, c), the lens sees the beam coming from a direction that is the backward prolongation of the asymptote of the deflected beam. Thus the adjustment of the lens for a straight image of the

magnetized wire (fig. 8, b) constitutes a rather simple criterion for the best possible focus. Although this is not an absolute criterion, eq 19 indicates that no appreciable errors are involved under the existing experimental conditions. It is possible, furthermore, that this effect may itself serve as a method for the quantitative evaluation of the field strength.

IV. Bright-Field Shadow Method for Quantitative Investigations

1. Description of the Method

In one of our Schlieren experiments described in the preceding section, it so happened that the shadow image of the center stop (produced on the screen by projection from the virtual source between the lens and the stop) was displaced laterally by means of an external deflecting magnetic field. By adjusting the image of one of the fine supporting silver wires to be parallel with the image of the magnetized wire, we found that the image of that silver wire was not straight but zigzag when in the neighborhood of the image of the magnetized wire.

This accidental observation gave rise to the new bright-field image method, mentioned in the introduction, for exploring the magnetic field. Extensive experiments with this method have indicated that it lends itself especially well to quantitative work. Insertion of a series of easily obtained experimental measurements into theoretically derived formulas has yielded fairly consistent values for the field strength, and close agreement with theory. Furthermore, the difficulties inherent in quantitative measurement of intensity patterns are not present in this method.

Figure 9 is a diagram of the arrangement used in this method. The diagram is in the equatorial plane of one of the dipoles comprising the magnetized wire,⁷ which is normal to the diagram and is centered about S' , the north pole being below the diagram, whose orientation is therefore the same as that of figures 1, 2, and 3. When the wire is not magnetized, parallel rays passing the wire are focused by the lens, whose principal planes are at P' , P , and cross over at the focus F , as illustrated. They are then partly blocked by the stop and its supporting silver wires, which are

⁷ The dipole assumption used here yields a first approximation. The extended results given in section V lead to greater accuracy.

in a plane through C . One of these cross-wires, GG_+ , is made parallel to the wire S' (normal to the diagram plane), so that its shadow TT_+ on the fluorescent screen S (conjugate to S') will be parallel to—and, for small displacements from the axis, hidden by—the image of the magnetized wire.

When the latter is magnetized, however, the resulting deflection of the incident beam is found to produce on the screen a zigzag cross-wire shadow of nonuniform width, whereas the magnetic wire image remains practically unchanged. (See fig. 10.) Measurements on this deformed shadow, for each silver wire displacement g , may be substituted into theoretical formulas yielding independent estimates of the dipole strength. The degree of consistency with which these data follow predicted laws serves as a measure of the applicability of the theoretical assumptions.

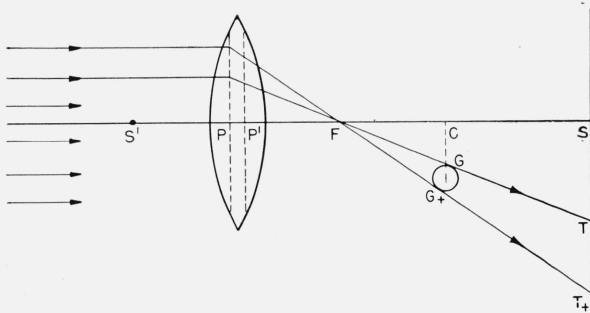


FIGURE 9. Electron optical diagram of arrangement used in bright-field method.

Displacement g of thin cross-wire GG_+ is adjustable. Rays shown apply in absence of magnetized wire S' .

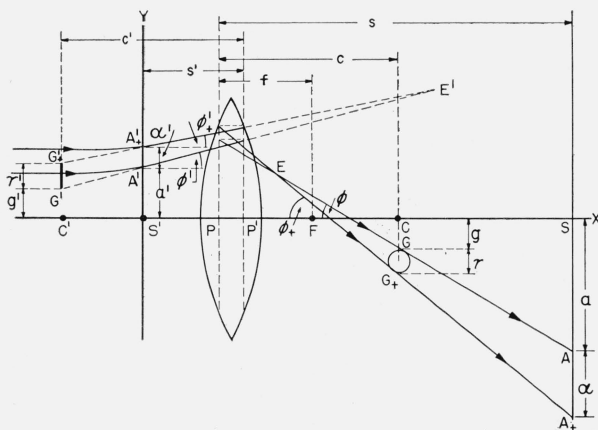


FIGURE 10. Detailed electron optical diagram of arrangement of figure 9, showing electron paths through deflecting field of magnetized wire S' in an equatorial plane.

2. Theoretical Analysis for Isolated Dipole

Figure 10 is similar to figure 9, except that S' now represents a magnetized dipole. The two curved rays represent portions of the paths of the limiting electrons which, after deflection by the magnetized wire S' , just pass the cross-wire GG_+ unblocked. The dashed lines $G'_+A'_+E'$, $G'A'E'$ are the asymptotes of these curved trajectories. *Primed* points and quantities represent *conjugates* of corresponding unprimed symbols with respect to the lens; points such as C' , G' , A' , A'_+ , and distances such as γ' , g' , α' , c' , are thus defined. All labeled distances are defined as positive when as in figure 10, and negative when in the opposite sense.

In addition to the ideal dipole assumption, the following experimental conditions regarding orders of magnitude are to be taken into account:

(a) The actual source is at a sufficiently great distance so that the net effect does not differ appreciably from that of the parallel incident beam of figures 9 and 10.

(b) All lateral distances and angles involved are sufficiently small to make geometrical aberrations negligible, so that Gaussian dioptrics is applicable.

(c) The distance s' is so large that the lens may be considered as outside the magnetic field.

By conditions (b) and (c) the rays EA_+ and EA (fig. 10) are straight lines and are conjugate to the asymptotes $E'A'_+$ and $E'A'$ with respect to the lens. Thus the effect of the magnetic field and distant source is equivalent to that of a virtual source at E' , defined as the point of intersection of the two limiting asymptotes. The resulting one-to-one correspondence reduces the analysis to a study of the geometry on the left-hand side of the lens. The geometry of the image is then obtained directly through the introduction of magnification factors.

By condition (b), furthermore, the points of tangency G and G_+ may be considered as being vertically in line with the point C on the optic axis.

The main part of the analysis that follows is the derivation of a field-strength formula based on the properties of the boundary ray $G'A'GA$ (fig. 10), which is characterized by the distance g . A similar result based on the other boundary ray, $G'_+A'_+G_+A_+$, is then obtained at once on replacing g by $g+\gamma$. The results are put in terms of

experimentally measurable quantities for numerical application (sec. IV, 3). They are then used to predict the behavior of the shadow image as the cross-wire is moved normal to the optic axis (sec. IV, 4), yielding means of checking the agreement between theory and experiment both qualitatively and quantitatively (see footnote 7).

The dipole trajectory formulas of section II can now be applied to figure 10. Since the polar orientation of the dipole with respect to the plane of the diagram is the same in figures 9 and 10 as in figure 1, $S'A'A'_+$ of figure 10 corresponds to the positive y -axis of figure 1. Hence for the ray $G'A'GA$ of figure 10, the notation of section II gives

$$\phi' = \tilde{\theta} \text{ and } a' = \tilde{y}. \quad (28)$$

But as was pointed out in section II, 2, indications are that the paths of all electrons that pass the magnetized wire correspond to large $|Y_0|$, for which simple approximate formulas are applicable. The paths involved in this experiment correspond to $|Y_0|$ so large that deviations from these approximate formulas are negligible. From eq 28 and the results of section II, then,—in particular eq 19, 17, and 4,—

$$a' = y_0; \quad (29)$$

$$\phi' = 2/Y_0^2 = 2B/a'^2 > 0; \quad (30)$$

$$a' - g' = \phi'(c' - s') > 0; \therefore \phi' = (a' - g')/(c' - s'). \quad (31)$$

Solving eq 30 for B and eliminating ϕ' through eq 31, we obtain the important formula

$$B = a'^2(a' - g')/2(c' - s'). \quad (32)$$

But B , as defined by eq (2), is a constant of the dipole and source, so that eq 32 should yield the same value of B for different values of g' . When B has been so determined, the magnetic moment M , and the field strength H at any distance r from the wire axis, can be obtained immediately from eq 3 and eq 1, which give

$$M = B\sqrt{2mV/e}, \text{ and } H = M/r^3. \quad (33)$$

For B in square millimeters, r in millimeters, and V in volts, H is given in oersteds by

$$H = 33.7BV^{1/2}/r^3. \quad (34a)$$

When $V = 40,000$ volts, as in the experiments, the field in oersteds at 0.1 mm from the wire axis (about two wire radii) is

$$H = 6.74 \times 10^6 B; \quad (34b)$$

at 0.2 mm it is one-eighth of this; etc.

The formula 32, when put in a form involving experimentally measurable quantities, and combined with eq 34, yields a numerical value for H based on the boundary ray $G'A'GA$ (fig. 10) alone. An exactly similar formula based on the other boundary ray $G'_+A'_+G_+A_+$ would be equally satisfactory:

$$B = (a' + \alpha')^2(a' + \alpha' - g' - \gamma')/2(c' - s') \\ = a'_+{}^2(a'_+ - g'_+)/2(c' - s'). \quad (35)$$

The second form of eq 35 involves the introduction of new notation:

$$g_+ = g + \gamma, \quad a_+ = a + \alpha, \quad g'_+ = g' + \gamma', \quad a'_+ = a' + \alpha', \\ \gamma_+ = -\gamma, \quad \alpha_+ = -\alpha, \quad \gamma'_+ = -\gamma', \quad \alpha'_+ = -\alpha'. \quad (36)$$

Use of this notation makes it possible to *interchange the roles of the two boundary rays* in any equation or statement, merely by inserting the subscript $+$ in the symbols g, γ, a, α , etc., wherever it is missing, and removing it wherever it appears.

Throughout section IV, 3 the possibility of such an interchange will be understood. Hence, although a large portion of the text treats explicitly only the ray $G'A'GA$, every statement involving that ray will contain implicitly an exactly analogous statement involving the ray $G'_+A'_+G_+A_+$.

3. Adaptation of Results to Experimental Conditions

Before translating eq 32 into a form for experimental use, we introduce some new notation. First, the analysis up to this point has been in the form of a study of deflections in the equatorial plane of an isolated dipole of known polarity. Actually the magnetized wire consists essentially of a series of dipoles (see footnote 7) of alternating polarity but approximately equal strength. Hence any configuration on the fluorescent screen will be a composite picture from which, in general, two basically different sets of measurements can be obtained: one set pertaining to the equatorial planes of the (approximately identical) dipoles of one polarity, and another corresponding set for the oppositely polarized dipoles. Certain distances

measured normal to the optic axis in figure 10 ($a, \alpha, a', \alpha', g, g'$) will not, in the general case, be the same for the two sets of dipoles. Subscripts 1 and 2, referring to the two opposing dipoles, will be appended to these quantities whenever it is desired to distinguish between them; but the decision as to which dipole polarity is to be assigned each subscript will be left arbitrary for the present.

A difficulty in notation is presented by the fact that figure 10 is oriented according to dipole polarity. This implies that the positive y -direction (normal to the optic axis) for one set of alternate dipoles will become the negative direction for the other set of dipoles, so that the composite image on the fluorescent screen will require a nonuniform sign convention. And if the displacements g and g_+ of the cross-wire edges G and G_+ , respectively, (fig. 10) are g_1 and g_{1+} when one specific dipole is considered, then for either adjacent dipole the corresponding displacements are

$$g_2 = -g_1, \text{ and } g_{2+} = -g_{1+}, \quad (37)$$

whence also, from eq 36,

$$\gamma_2 = -\gamma_1 = \gamma_{1+} = -\gamma_{2+}. \quad (38)$$

To eliminate these difficulties we arbitrarily define *starred* quantities as follows:

$$g^* = g_1 = -g_2; a_1^* = a_1; a_2^* = -a_2; \alpha_1^* = \alpha_1; \alpha_2^* = -\alpha_2; \gamma^* = \gamma_1 = -\gamma_2 = -\gamma_{1+} = \gamma_{2+} = -\gamma_{2+}^*; \text{ etc.} \quad (39)$$

Thus *starred* quantities have the same *magnitudes* as corresponding unstarred quantities, whereas their algebraic *signs* are determined by dipoles of the first polarity (subscript 1) and are therefore reversed for quantities with subscript 2. If a coordinate system is set up on the fluorescent screen, the use of starred quantities implies a uniform sign convention throughout the screen; a_1^* and a_2^* are then the ordinates of one rim of the shadow at its intersection with the equatorial planes of alternate dipoles, as shown in figure 11.

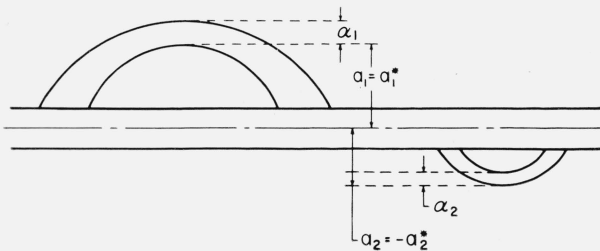


FIGURE 11. Diagram of a typical bright-field shadow of cross-wire.

Straight band is image of magnetized wire.

Finally, in order to introduce experimentally measurable quantities into eq 32, we define several *magnifications*:

$$\mu = s/s' = \text{magnification of magnetized wire image on screen}; \quad (40)$$

$$\nu = (s-f)/(c-f) = TT_+/GG_+ \text{ (fig. 9)} \quad (41)$$

= magnification of silver wire as determined by its shadow on screen *in absence of magnetic field*;

$$n_i = \alpha_i/\gamma = \alpha_{i+}/\gamma_+ \quad (42)$$

= corresponding shadow magnification *in presence of magnetic field* ($i=1,2$);

$$\omega = c/c' = \gamma/\gamma' = g/g' \quad (43)$$

= magnification associated with cross-wire plane CGG_+ and its conjugate plane $C'G'G'_+$.

Ordinarily only μ and ν will be known experimentally, the others being obtainable therefrom, as will be shown.

From eq 40 and 43, and the image formula $1/s + 1/s' = 1/c' + 1/c = 1/f$, we obtain

$$c = f(1 + \omega), \quad s = f(1 + \mu), \quad (44)$$

whence eq 41 yields a simple formula for ω in terms of μ and ν :

$$\omega = \mu/\nu. \quad (45)$$

Equations 39–45 yields the relations

$$a'_1 = a_1^*/\mu, \quad a'_2 = -a_2^*/\mu, \quad g'_1 = -g'_2 = g^*/\omega = g^*\nu/\mu; \quad s' = s/\mu = f(1 + 1/\mu); \quad c' = c/\omega = f(1 + \nu/\mu), \quad (46)$$

from which eq 32 may be put in terms of measurements on the fluorescent screen:

$$B = a_1^{*2}(a_1^* - \nu g^*)/2\mu^2(\nu - 1)f, \quad (47a)$$

and

$$B = a_2^{*2}(\nu g^* - a_2^*)/2\mu^2(\nu - 1)f. \quad (47b)$$

Two additional formulas, from measurements on the other boundary ray, are implied by eq 36:

$$B = a_{1+}^{*2}(a_{1+}^* - \nu g_{1+}^*)/2\mu^2(\nu - 1)f, \quad (47c)$$

$$B = a_{2+}^{*2}(\nu g_{2+}^* - a_{2+}^*)/2\mu^2(\nu - 1)f, \quad (47d)$$

where $g_{\pm}^* = g^* + \gamma^*$.

Equations 47 will, in general, give four independent estimates of B from a single composite

image, using measurements on the displacements of both edges of the shadow and for dipoles of both orientations, provided the displacement g^* is known. For certain special cases, however, the number of independent results obtained from eq 47 is reduced or increased.

(Case 1) When, as in the experiments described herein, the displacements g^* and g_+ are not known accurately, they may be determined algebraically by solving the eq 47 simultaneously in pairs, whereupon the four equations yield but two completely independent estimates. When the cross-wire thickness $\gamma^* = g_+^* - g^*$ is known, three independent estimates are possible.

(Case 2) Under certain conditions a double or triple shadow appears, as shown in the next section, yielding additional independent measurements.

(Case 3) For the symmetric case, for which the cross-wire is centered on the optic (x -) axis, we have

$$g_+^* = -g^* = \gamma^*/2, \quad (48)$$

$$a_{1+}^* = a_2^*, \quad (49)$$

$$a_{2+}^* = -a_1^*, \quad (50)$$

so that eq 47a and 47d are identical, as are also eq 47b and 47c.

(Case 4) For the case for which the cross-wire is tangent to the optic axis, we have

$$g^* = 0, \quad a_1^* = -a_2^* = a_0, \quad (51)$$

so that both eq 47a and 47b reduce to

$$B = a_0^3/2\mu^2(\nu - 1)f. \quad (52)$$

(Case 5) When the cross-wire shadow is thin in comparison with its displacement, i. e., when $|\alpha_i| \ll |a_i|$, then $a_1^* \approx a_{1+}^*$, $a_2^* \approx a_{2+}^*$, $g^* \approx g_+$, so that eq 47c and 47d are approximately identical with eq 47a and 47b respectively, and therefore cannot be considered as independent in numerical work. In this case, however, in place of eq 47c and 47d, two other equations

$$\alpha_i = \nu\gamma/(3 - 2\nu g^*/a_i^*), \quad i=1,2, \quad (53)$$

may be used for independent checks on eq 47a and 47b. These are expressions for the *shadow thicknesses*, obtained by differentiation of eq 47a and 47b, with

$$dg_i = \gamma, \quad da_i = \alpha_i, \quad da_i^* = \alpha_i^* (i=1,2), \quad dB \equiv 0. \quad (54)$$

An evaluation of B from a screen image by means of eq 47 requires only the two measurements a_1^* and a_2^* , the displacements of one shadow edge from the axis of the magnetized wire image at the centers of alternate magnetized regions. The focal length f and the magnifications μ and ν may be determined from independent measurements. In particular ν , the shadow-magnification for an undeflected beam, may be determined accurately from the shadow of the center-stop disk itself instead of that of its fine supporting wires.

The value of B so determined, and the known electron accelerating voltage V , may then be substituted directly into eq 34 for a determination of the field strength H at any specified distance r from the magnetized wire axis.

The value of B determined by eq 47 may be verified by any or all of the following methods:

(a) For thick shadows, the calculation from eq 47a, b may be repeated using the measurements a_{1+}^* and a_{2+}^* , for the other shadow edge, as in eq 47c, d.

(b) For thin shadows (Case 5 above) the differential formulas (eq 53) may be checked against measurements on the shadow thicknesses α_1 and α_2 . The numerical agreement of each of these is equivalent to an independent check on B .

(c) The above calculations may be applied to several photographs corresponding to different cross-wire displacements g^* . Results may be averaged, and their range of variation used as an indicator of the accuracy of the final figure.

4. Shadow Form as Function of Cross-Wire Displacement

A theoretical investigation is now made of the manner in which the shadow moves along the fluorescent screen and in which its thickness changes, as the silver wire is moved across and beyond the optic axis; i. e., the functional dependence of a and α on g will be studied. Certain recognizable peculiarities in the shadow behavior afford a qualitative check between experimental conditions and theoretical assumptions, while additional quantitative predictions are also obtained.

As in Figure 10, suppose the rim G of the silver cross-wire to be displaced a distance g^* from the optic axis, with resulting shadow-rim displacements $a_1^* = a_1^*(g^*)$, $a_2^* = a_2^*(g^*)$ and shadow thicknesses $\alpha_1 = \alpha_1(g^*) = a_1^*(g^* + \gamma^*) - a_1^*(g^*)$, and

$\alpha_2 = \alpha_2(g^*) = a_2^*(g^*) - a_2^*(g^* + \gamma^*)$, at points corresponding to alternate equatorial planes; and let

$$a_0 = a_1^*(0) = -a_2^*(0), \quad \alpha_0 = \alpha_1(0) = \alpha_2(0), \quad (55)$$

be the corresponding values of these quantities when $g^* = 0$. Then by eq 47 and 52, $a_1^{*2}(a_1^* - \nu g^*) = a_2^{*2}(\nu g^* - a_2^*) = a_0^3 = 2\mu_2(\nu - 1)fB = \text{constant}$, or

$$\frac{\nu}{a_0} g^* = \frac{a_1^*}{a_0} - \left(\frac{a_1^*}{a_0}\right)^{-2}, \quad \text{also} \quad \frac{\nu}{a_0} g^* = \frac{a_2^*}{a_0} + \left(\frac{a_2^*}{a_0}\right)^{-2}, \quad (56)$$

where

$$a_0 = [2\mu^2(\nu - 1)fB]^{1/3} = \text{constant}. \quad (57)$$

Thus g^* is related to both a_1^* and a_2^* by cubic equations, which if solved may make the a_1^* triple-valued functions of g^* in some intervals, and single-valued functions elsewhere.

Figure 12, based on eq 56, is a plot of the deflections a_i^* (in normalized form a_i^*/a_0) of the shadow rim A , as functions of g^* (in normalized form $\nu g^*/a_0$). The deflections a_{i+}^* of the other shadow rim A_+ are identical functions of $g_+^* = g^* + \gamma^*$. This graph may be interpreted as predicting theoretically the form of the zigzag shadow image on the screen, corresponding to a given g^* . With this given g^* as abscissa, the ordinate a_1^* determined by the curve marked " $i=1$ " in figure 12 represents the *maximum displacement* of the edge of the zigzag image, as measured from the image of the magnetized wire axis as a coordinate axis; such a maximum displacement occurs at points along this axis corresponding to the equatorial planes of the dipoles of a particular polarity. Similarly the ordinate a_2^* determined by the curve marked " $i=2$ " represents the displacement of the same shadow edge at the intermediate points (centers of the dipoles of opposite polarity).⁸ (The two displacements of the other shadow edge are given by corresponding ordinates with $g_+^* = g^* + \gamma^*$ as abscissa).

These two displacements are equal and opposite when $g^* = 0$, and approach coincidence (straight shadow) as g^* becomes large. For intermediate values of g^* figure 12 shows a peculiar behavior of the shadow. For $\nu g^*/a_0 < 1.89 (= 3 \times 2^{-2/3})$ the two displacements are on opposite sides, i. e., $a_2^* < 0$. As g^* passes this critical value, indicated

⁸ Although the curves are plotted for positive g^* only, those for negative g^* (seldom needed—see end of first paragraph of sec. IV, 3) are obtained by changing the signs of both coordinates while interchanging " $i=1$ " and " $i=2$ " curves.

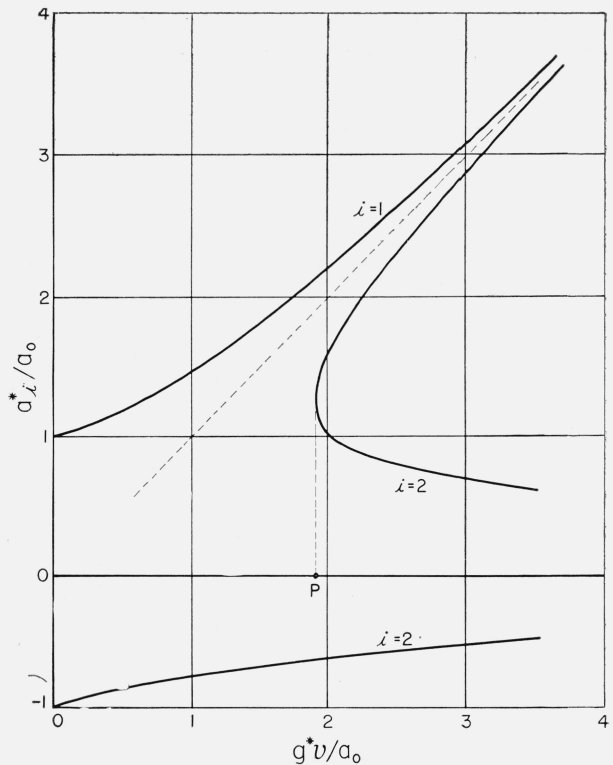


FIGURE 12. Displacements a_i^* (normalized) of shadow edge on screen, in equatorial planes, as functions of displacement g^* (normalized) of corresponding edge of cross-wire itself.

by the point P , two new branches of the " $i=2$ " curve appear, and a_2^* becomes triple-valued, so that they are actually *three* shadow images for dipoles of the second polarity. Although one of these images is usually hidden by the magnetized wire image, whose half-thickness is of the order of $0.5 a_0$ in these experiments, the appearance of two others instead of the usual single image yields an additional independent estimate of B . As g^* increases further, however, this additional image disappears behind the magnetized wire image, leaving only the outermost image, on which the effect of the magnetic field becomes less and less marked.

There remains the analysis of shadow *thickness* and magnification. For a *thick* shadow, the thicknesses α_i^* are obtained from figure 12 as differences Δa_i^* between ordinates corresponding to abscissa differences $\Delta g^* = \gamma^*$, $|\gamma^*|$ being the cross-wire diameter; and the corresponding shadow magnifications $n_i = \alpha_i^*/\gamma^*$, as defined by eq 42, are proportional to these thicknesses. In fact, the magnification ratio n_i/ν , expressing the shadow magnification in the presence of the field in units

of that obtained with zero field, is obtained directly (and in proper units) as the slope of the chord joining the two relevant points on the appropriate curve of figure 12. For such a slope is of the form

$$\Delta(a_i^*/a_0)/\Delta(\nu g^*/a_0) = \alpha_i^*/\nu\gamma^* = n_i/\nu. \quad (58)$$

For a shadow so thin, however, that γ^* and α^* are of differential magnitude (Case 5 above), the two points implied by eq 58 are so close together that a good approximation of n_i/ν is given by the instantaneous slope of the curve at the abscissa g^* or g_+^* . This slope is given analytically by eq 53, which, with the aid of eq 42 and 56, may be put into the form

$$\begin{aligned} n_1/\nu &= \alpha_1/\nu\gamma = 1/[1 + 2(a_1^*/a_0)^{-3}]; \\ n_2/\nu &= \alpha_2/\nu\gamma = 1/[1 - 2(a_2^*/a_0)^{-3}]. \end{aligned} \quad (59)$$

Combination of these with eq 56 yields n_1 and n_2 (also α_1 and α_2) as functions of g^* for a thin shadow. Figure 13, based on eq 59, is a plot of the shadow magnifications n_i or thicknesses α_i (in normalized form n_i/ν) versus g^* (in normalized form $\nu g^*/a_0$). It is essentially a plot of the derivatives of the functions of figure 12.

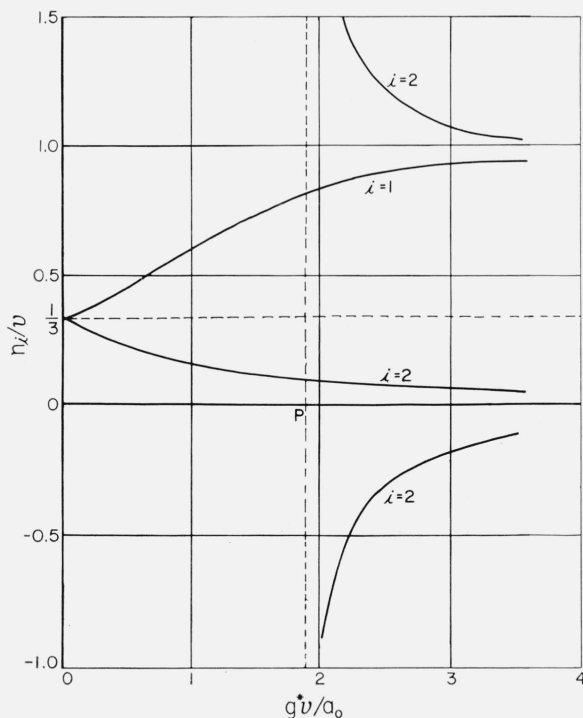


FIGURE 13. Magnifications n_i (normalized) of thin shadow, in equatorial planes, as functions of displacement g^* (normalized).

An important theoretical conclusion from eq 59 concerns the magnification n_0 of a very thin cross-wire centered about the optic axis. Here g^* and g_+^* differ negligibly from zero, so that eq 59 and 51 yield

$$n_0/\nu = 1/3; \quad (60)$$

i. e., when an infinitesimally thin cross-wire is centered (i. e., $g^*=0$) the shadow magnification n_0 is exactly one third of its value ν in the absence of the field. This implies, in figures 9 and 10, that $TT_+ = 3\alpha$, and that the cross-over E (projected on the optic axis) is twice as far behind the focus F as the cross-wire C is beyond it, when the latter is centered. It also implies that α_0 of eq 55 is equal to $\nu\gamma/3$.

Figure 13 shows the manner in which the two n_i for a thin shadow vary from $\nu/3$, at $g^*=0$, to ν as $g^*\rightarrow\infty$. The three magnifications n_2 beyond the critical point P refer to the three images indicated by figure 12. The magnification is infinite at the critical point P ($g^*=1.89$). Negative magnifications imply an inverted shadow, and a cross-over between cross-wire and screen.

5. Qualitative Experimental Results

The apparatus used in the bright-field method experiments is essentially the same as the Schlieren apparatus described in section III, 3. The latter, together with the introductory remarks in section IV, 1 describing the rearrangement, should constitute a sufficient description of the experimental procedure involved.

Figures 14 and 15 are (magnification approximately $\times 3$) configurations on the fluorescent screen for different silver wire positions. The wide dark band is the image of the magnetized wire, whereas the thinner, distorted band is the shadow image of the cross-wire. In figure 14, A the cross-wire is sufficiently far from the optic axis so that its shadow has negligible curvature; whereas figure 14, B and C shows the result of moving the cross-wire closer to the optic axis, until the central position ($g^*\approx -g_+^*$) is approximately reached in figure 14, c. Figures 15, a and b are similar to figures 14, b and c but involve somewhat different physical parameters. (A portion of a dark circle appearing on the side of some of the photographs is part of the shadow of the center stop itself.) The turning points, i. e.,

points of maximum and minimum deflection of the shadow, correspond to the equatorial planes of the dipoles (magnetized regions).

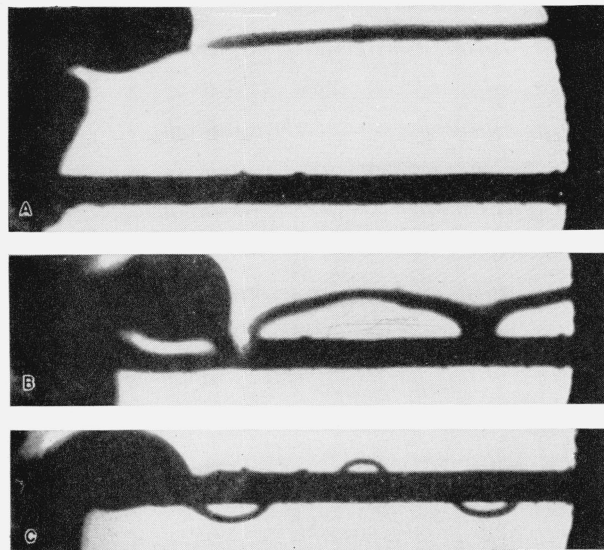


FIGURE 14. Shadow patterns showing distorted shadow of cross-wire and electron optical image of magnetized wire (straight wide band).

Light optical magnification about $\times 3$. (A) Cross-wire at great distance g^* from optic axis; shadow practically straight. (B) Cross-wire at smaller but appreciable distance g^* from optic axis. (C) Cross-wire approximately centered on optic axis ($g^* \approx 0$).

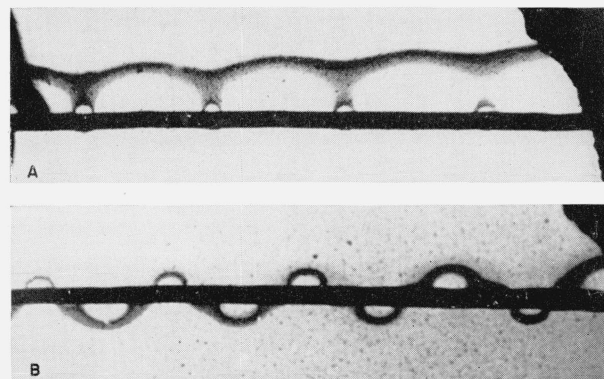


FIGURE 15. Shadow patterns similar to figure 14 but with different electron optical parameters.

These figures can be seen to agree well, qualitatively at least, with the theoretical curves of figures 12 and 13. Each photograph corresponds to a particular abscissa g^* on those graphs, or more precisely, to two abscissas g^* and g_+^* for the two edges of the cross-wire. In accordance with figure 13, when the shadow bulges out on both sides of the central image (figs. 14, C and 15, B) it is thicker

on the side that shows the greater bulges; and these thicknesses appear to be of the order of one-half—somewhat greater than the theoretically predicted one-third—of that of the straight shadow of figure 14, a. The discrepancy seems to be explained by the results of the next section.

Of particular interest are figures 14, b and 15, a—figure 15, a being by far the clearer—which follow very closely the theoretical predictions of section IV, 4 regarding the peculiar behavior of the shadow in the vicinity of the critical point P of figures 12 and 13. Not only (a) the extreme thickness of the shadow at alternate equatorial planes in figure 15, a, but also (b) the small bright spot bounded by the thick shadow and the magnetized wire image, and (c) the very slight but distinct bulging on the opposite side of this central image, are explained by the “ $i=2$ ” curves of figure 12, which indicate that these photographs correspond to a cross-wire displacement such that the upper edge of the cross-wire corresponds to a g^* to the right of the point P , whereas the g_+^* for the lower edge lies to the left of P . Both the outer boundary of the thick shadow and the outer boundary of the bright spot are shadows of the upper edge, with no corresponding shadows of the lower edge.⁹ Furthermore, the bulging on the opposite side of the central image represents part of the third shadow, shown by the negative branch of the curve in figure 12.

This apparent qualitative agreement of theory and experiment may be interpreted as a tentative verification of the ideal-dipole assumption as a first approximation. For a more accurate approximation, section V introduces a new parameter, and more positive results are obtained in section VI, in which the quantitative data are analyzed.

V. Correction for Magnet Length

The analysis up to this point has been based on the assumption that the elementary magnets of the wire are ideal dipoles. Although this assumption may be expected to yield results of the correct order of magnitude, the main limitation on their accuracy is due to the fact that a theoretical dipole is infinitesimally short. In these experiments measurements were taken at small distances, com-

⁹ Due to a slight nonparallelism, one of these thick shadows in figure 15, a is in fact broken, the two boundaries of the break being shadows of the lower edge.

parable with the magnet length, which by figure 7, b is about two wire diameters.

A considerably better approximation, therefore, may be expected if one assumes the form of the field to be that of *two equal and opposite point poles* separated by some distance 2λ . As $\lambda \rightarrow 0$ this reduces to the dipole assumption, whereas the additional parameter λ introduced yields one more degree of freedom. A method is derived whereby the equivalent pole separation 2λ for the wire magnets is evaluated in the process of determining H .

The effects of this generalization of the basic assumption on the preceding analytical results are summarized below. Each equation having a direct analog in the earlier sections is numbered with a prime, implying a reference, for comparison, to the equation bearing the corresponding unprimed number.

Exact analysis (sec. II, 1):

The field distribution in the equatorial plane of the magnet is now

$$H = M/\mu'(r^2 + \lambda^2)^{3/2} = M/\mu'\bar{r}^3, \quad (1')$$

where $\bar{r} = \sqrt{r^2 + \lambda^2}$ = distance from either pole to (r, θ) in equatorial plane.

The exact differential equation of motion is not as simple as earlier. If, however, we define

$$\Lambda = \lambda/\sqrt{B}, \quad \bar{R} = (R^2 + \Lambda^2)^{1/2}, \quad \bar{Y} = (Y^2 + \Lambda^2)^{1/2},$$

the exact solution (eq 5) becomes an approximate solution for the new case when R and Y_0 are replaced throughout by some variables \bar{R} and \bar{Y}_0 , where $R < \bar{R} < \bar{R}$, $Y_0 < \bar{Y}_0 < \bar{Y}_0$.

Small-deflection approximations (sec. II, 2):

For large \bar{Y}_0 the final deflection now becomes

$$\tilde{\theta} \approx 2/\bar{Y}_0^2 = 2/(Y_0^2 + \Lambda^2), \quad (17')$$

and the equation of the final asymptote

$$Y = Y_0 + 2X/(Y_0^2 + \Lambda^2). \quad (18')$$

Theoretical Schlieren analysis (sec. III, 2):

Inequalities 26 and 27 for the predicted limits on the pattern become respectively

$$\begin{aligned} Y_{\min} + 2X_L/(Y_{\min}^2 + \Lambda^2) + R_L &= 0, \\ Y_{\max} + 2X_L/(Y_{\max}^2 + \Lambda^2) - R_L &= 0, \end{aligned} \quad (26')$$

and

$$Y_{\min} \approx -\sqrt{\Lambda^2 + 2f/r_c}, \quad Y_{\max} \approx +\sqrt{\Lambda^2 + 2f/r_c}. \quad (27')$$

Determination of H by bright-field method (secs. IV, 2; IV, 3):

The formulas (eq 32 and 35) for B become

$$B = (a'^2 + \lambda^2)(a' - g')/2(c' - s') \quad (32')$$

$$= (a'_+{}^2 + \lambda^2)(a'_+ - g'_+)/2(c' - s'). \quad (35')$$

The formula (eq 34a) for determining H from B becomes

$$H = 33.7 B^{1/2}/(r^2 + \lambda^2)^{3/2}. \quad (34')$$

In terms of measurements on the screen,

$$B = (a_1^{*2} + \mu^2\lambda^2)(a_1^* - \nu g^*)/2\mu^2(\nu - 1)f, \quad (47a')$$

and

$$B = (a_2^{*2} + \mu^2\lambda^2)(\nu g^* - a_2^*)/2\mu^2(\nu - 1)f, \quad (47b')$$

with similar expressions at the other boundary as in eq 47c and 47d.

The shadow thicknesses α_1, α_2 obtained by differentiation for thin shadows become

$$\alpha_i = \nu\gamma[1 + (\mu\lambda/a_i^*)^2]/[3 + (\mu\lambda/a_i^*)^2 - 2\nu g^*/a_i^*], \quad i=1, 2. \quad (53')$$

Shadow form as function of cross-wire displacement (sec. IV, 4):

The relations (eq 56) between g^* and a_i^* become

$$\left. \begin{aligned} \nu g^*/a_0 &= a_1^*/a_0 - (a_1^*/a_0)^{-2}/[1 + (\mu\lambda/a_0)^2(a_1^*/a_0)^{-2}], \\ \nu g^*/a_0 &= a_2^*/a_0 + (a_2^*/a_0)^{-2}/[1 + (\mu\lambda/a_0)^2(a_2^*/a_0)^{-2}], \end{aligned} \right\} \quad (56')$$

where a_0 is considered as defined by eq 57 rather than by eq 55.

The corresponding magnifications n_1, n_2 of thin shadows become

$$\left. \begin{aligned} n_1/\nu &= \alpha_1/\nu\gamma \\ &= 1/\{1 + 2(a_1^*/a_0)[(a_1^*/a_0)^2 + (\mu\lambda/a_0)^2]^{-2}\}; \\ n_2/\nu &= \alpha_2/\nu\gamma \\ &= 1/\{1 - 2(a_2^*/a_0)[(a_2^*/a_0)^2 + (\mu\lambda/a_0)^2]^{-2}\}. \end{aligned} \right\} \quad (59')$$

In place of eq 60, for the case of a very thin cross-wire centered about the optic axis,

$$n_0/\nu = [1 + (\mu\lambda/a_1^*)^2]/[3 + (\mu\lambda/a_1^*)^2]. \quad (60')$$

The effect of these changes on figures 12 and 13 is in a direction indicating considerably better

agreement between observation and theory, as will be shown in the next section, in which the theoretical and experimental shadow magnifications are compared.

VI. Quantitative Results

The general equations¹⁰ (eq 47') for B , on the generalized hypothesis of section V, may be written

$$B = w + \lambda^2 u, \quad (61)$$

where, on this hypothesis, B and λ are constants of the wire, whereas w and u are variables:

$$\left. \begin{aligned} w &= a_i^{*2} |a_i^* - \nu g^*| / 2\mu^2 (\nu - 1) f, \quad (i=1 \text{ or } 2). \\ u &= |a_i^* - \nu g^*| / 2(\nu - 1) f. \end{aligned} \right\} \quad (62)$$

In any photograph, each measurement of the displacement of a shadow boundary, in the equatorial plane of a dipole of either polarity, yields a pair of experimental values of u and w , provided the displacement g^* has been determined. Equation 61 implies that under the generalized hypothesis these points should lie on a straight line whose slope and w -intercept are $(-\lambda^2)$ and B respectively.

On the earlier hypothesis of an ideal dipole, however, the equations (47) for B take the form

$$B = w, \quad (63)$$

implying that the same experimental points would lie along a *horizontal* line if the dipole case were applicable.

Figure 16 shows a plot of 22 experimental points (u , w) obtained from shadow-edge displacement measurements in different portions of figures 14 and 15. In each case g^* was determined by equating the values of the right member of eq 61 at two values of a_i , so that the two points so obtained are not entirely independent of each other, and each is given only half weight in all averaging. The 18 singly encircled points in figure 16 form 9 such pairs, whereas each of the 4 doubly encircled points represents an entirely independent measurement; the 22 points are thus equivalent to 13 mutually independent measurements.

¹⁰ All primed equation numbers appear in section V.

The solid line, fitted to the points by least squares, has a slope

$$-\lambda^2 = -0.00790 \text{ mm}^2, \quad (64)$$

and a w -intercept

$$B = 2.14 \times 10^{-5} \text{ mm}^2. \quad (65)$$

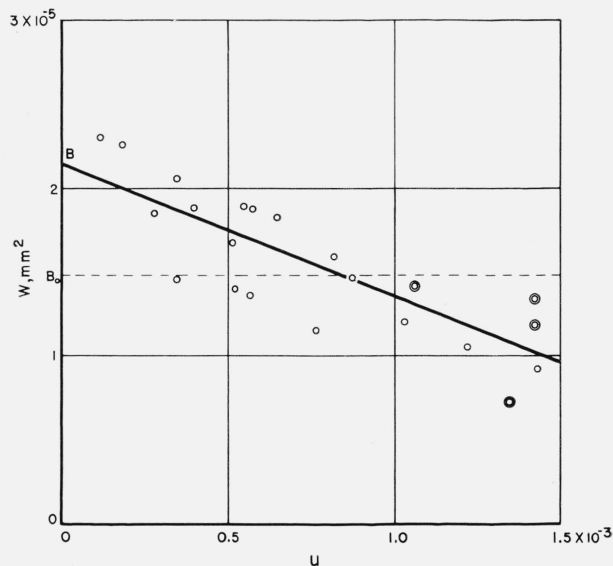


FIGURE 16. Plot of experimental measurements, and fitted theoretical lines, for determination of wire parameters B and λ required for evaluation of field strength.

These are therefore the parameter values obtained on the hypothesis that the field is that of two point poles separated by a distance 2λ . From eq 64, this *equivalent pole separation* is

$$2\lambda = 0.178 \text{ mm} = 1.5 \text{ magnetized wire diameters}. \quad (66)$$

This agrees well with figure 7, b, showing actual elementary magnets about two diameters long, and hence places each equivalent point pole about one-fourth of the way in from extremity to center of the magnet.

From eq 65 and 34' one obtains a magnetic field (in oersteds; r in millimeters)

$$H = 0.144 / (r^2 + 0.0079)^{3/2}. \quad (67)$$

This distribution is plotted in figure 17. At 0.1 mm from the wire axis, or about 0.04 mm from the wire surface, it has a value of 60 oersteds.

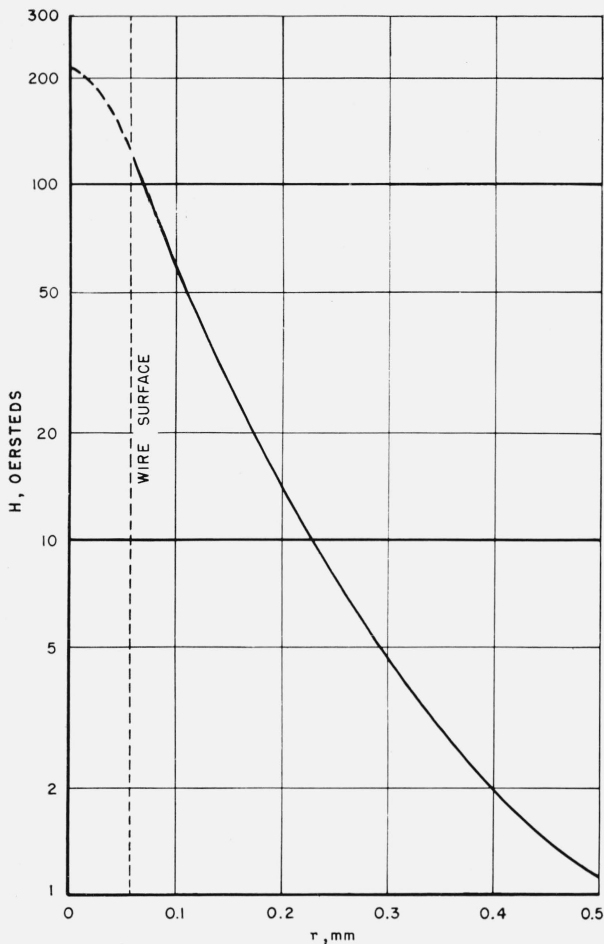


FIGURE 17. Theoretical field distribution of magnetized wire on hypothesis of section V, based on data in figure 16. (r = distance from wire axis.)

Curve is meaningless for $r \leq$ wire radius.

The degree to which the correction for magnet length improves the accuracy of the results is seen by comparing the solid line in figure 16 with the broken horizontal line obtained by simply averaging the ordinates of the points (see eq 63). This shows that the dipole hypothesis (without correction) would yield a value $B_0 = 1.48 \times 10^{-5}$ mm², which is 30 percent less than the B of eq 65. The very pronounced slope of the solid line, with relatively low standard deviation therefrom, is an indicator of the extent to which experimental conditions approximate the generalized hypothesis.

Further verification of the hypothesis is provided by a comparison of the actual shadow thickness with that predicted by eq 59'. It is to be noted that the magnification ratios for figures

14, c and 15, b in the following table would be only about 0.33 according to the original dipole hypothesis.

Figure number	i	Magnification ratio (n_i/v)	
		Theoretical	Measured
14, b	1	0.814	0.818
14, c	1	.492	.515
14, c	2	.447	.435
15, a	1	.832	.841
15, b (averaged)	1	.432	.400
15, b (averaged)	2	.344	.370

Finally, from eq 65, one obtains for the normalizing unit of length used in sections II and III,

$$\sqrt{B} = 0.0046 \text{ mm,}$$

which is about one-thirteenth of the wire radius, thus justifying the small-deflection approximations used.

VII. Conclusion

Although the preceding description refers to a very special application of the electron optical Schlieren and related methods, these methods are capable of wide application to the observation and measurement of electric and magnetic fields not susceptible to investigation by established techniques (see footnote 1). Other examples, in some of which preliminary experiments have been undertaken, are space charge fields, standing electromagnetic waves, time-varying fields, and ferromagnetic domains.

Essentially, the methods introduce a new category of objects to observation by means of electron optical systems. In the past, electron optics has been used to observe or to form images of two types of "objects":

(1) Objects emitting electrons, whereby the image is used for the study of surface properties and emission phenomena.

(2) Observation by scattered electrons, in which case the image formation shows differences in the scattering properties of different parts of the object and is therefore confined to observations of "transparent" or "translucent" objects.

To these two categories we now add a third category of objects: electromagnetic fields. The methods here described are essentially methods designed to form visible images of field distributions and to interpret them.

The authors acknowledge the assistance of Irvin L. Cooter, of the Magnetic Measurements

Section, who prepared the wire samples and furnished important information on their properties; Daniel L. Reverdin and John A. Simpson, who conducted additional experiments to provide supplementary data; and Andrew A. Nargizian, who carried out the extensive photographic measurements and numerical calculations leading to the set of final results.

WASHINGTON, April 15, 1949.

